Nanoscale

Accepted Manuscript

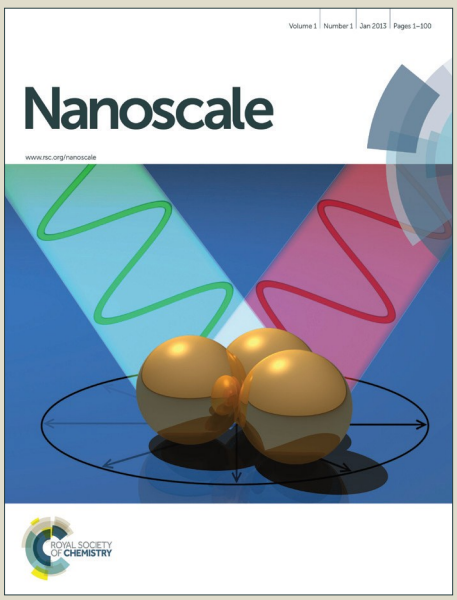

ROYAL SOCIETY OF CHEMISTRY

www.rsc.org/nanoscale

Nanoscale

PAPER

Interlinked multiphase Fe-doped MnO_2 nanostructures: a novel design for enhanced pseudocapacitive performance

Received 00th January 20xx,
Accepted 00th January 20xx

DOI: 10.1039/x0xx00000x

www.rsc.org/

Ziya Wang,[a] Fengping Wang,*[a] Yan Li,[a] Jianlin Hu,[a] Yanzhen Lu[a] and Mei Xu[a]

Structure design and morphology control can lead to high performance pseudocapacitive materials for supercapacitors. In this work, we have designed the interlinked multiphase Fe-doped MnO_2 nanostructures (α-MnO_2/R-MnO_2/ε-MnO_2) for enhancing the electrochemical properties by a facile way. These hierarchical hollow microspheres assembled by interconnected nanoflakes, and with plenty of porous nanorods radiating from the spherical shells were hydrothermally obtained. The supercapacitor electrode prepared from the unique construction exhibits outstanding specific capacitance of 267.0 F g^{-1} even under a high mass loading (~5 mg cm^{-2}). Obviously improved performances compared to pure MnO_2 is also demonstrated with a good rate capability, high energy density (1.30 mW h cm^{-3}) and excellent cycling stability of 100% capacitance retention after 2000 cycles at 2 A g^{-1}. The synergistic effects of alternative crystal structures, appropriate crystallinity and optimal morphology are identified to be responsible for the observations. This rational multiphase composite strategy provides a promising idea for materials scientists to design and prepare scalable electrode materials for energy storage devices.

Introduction

Supercapacitors are regarded as a greatly promising candidate for electrochemical energy storage and conversion due to their capability of fast energy delivery and ultralong cycle life. [1] In a traditional electric double layer capacitor (EDLC), energy is physically stored by adsorbing-desorbing charged ions from an electrolyte onto the surface of carbon material electrodes. [2] However, it is still limited by relatively low capacitance leading to low energy density, which seriously narrows the application range. [3, 4] Compared with various forms of carbon materials, pseudocapacitor materials can store much more energy via fast and reversible electrochemical redox reaction take place on the electrode surface. [5, 6] Therefore, it is essential to design and develop a pseudocapacitor electrode for retaining its intrinsic high power density and cyclability while enhancing the energy density. Up to now, the remarkable progresses of various pseudocapacitor materials containing transition metal oxides/hydroxides, [7, 8] metal sulfides/selenides, [9, 10] metal carbides/nitrides, [11, 12] binary metal oxides [13] and conducting polymers [14] have been explored and reported.

Manganese oxide (MnO_2) is one of the most capable transition metal oxides for pseudocapacitors due to high theoretical capacitance (1370 F g^{-1}), multiple valences, natural abundance and environmental friendliness. [15, 16] The capacitance of MnO_2 is attributed to reversible redox reaction including kinetic ion exchange with electrolyte cations and fast electron transport. [17] It suggests that MnO_2 must have high ionic and electronic conductivity. [4] Currently, MnO_2 has been widely investigated as electrode material for supercapacitors by a nanostructural design to increase the specific surface area accessible to the electrolyte. [18] However, MnO_2 intrinsically exhibits a relatively low conductivity (10^{-4}-10^{-3} S m^{-1}). [19] In this regard, the most popular solution is hybridizing with the high conductive scaffold (such as graphene and their derivatives), [20] and surface modification with conducting polymers. [19] While compared with these "surgery-like" methods which restricted by the MnO_2/external conductive reinforcements interfaces, doping nanoparticles (such as Co, Ni, Al, Fe, Ag and Au) into MnO_2 will more essentially increase the conductivity. [21-24] The free electron metal atoms as electron donors look forward to change the electronic structure of MnO_2. [23]

On this basis, three factors affecting the pseudocapacitance of MnO_2 materials also should be deliberated. [4, 25] First, alternative crystal structures. It is known that there are abundant types of crystallized MnO_2 (including α-, β-, γ- and so on), whose structural frameworks consist of [MnO_6] octahedral subunits sharing vertices and edges [26] and can be described by the size of their tunnel determined by the number of octahedral subunits (n×m). To date, various single-phase MnO_2 have been well studied. Second, appropriate crystallinity. High crystallinity materials with a higher conductivity will lower the polarization and accelerate the reaction kinetics, but low crystallinity commonly generates a highly porous microstructure, which facilitates the sufficient contact between electrolyte and active materials and shortens the ion

[a] Department of Physics, School of Mathematics and Physics, University of Science and Technology Beijing, Beijing, PR China. Corresponding author E-mail address: fpwang@ustb.edu.cn (F. Wang)

† Electronic Supplementary Information (ESI) available. See DOI: 10.1039/x0xx00000x

transport path. [4] Third, optimal morphology. The morphology of MnO_2 not only closely defines the microstructural stability (means long life span), but also determines the specific surface area which implies more faradaic active sites and thereby higher pseudocapacitance. [27] In all, the better supercapacitive performances come with the trade-off of every factors controlled by altering the preparation processes or reaction conditions.

According to previous studies and theoretical calculations, Fe dopants can substitute Mn or occupy the tunnels of MnO_2 easily due to the similar atomic radius of Fe^{3+} and Mn^{4+}. [28] Furthermore, appropriate Fe^{3+} incorporated into the MnO_2 frame work is highly beneficial to the balance of surplus protonation, thereby stabilizing the tunnel structures. [4, 29] Based on the above considerations, herein, we proposed a promising way to design a highly conductive MnO_2 material with rational heterogeneity, numerous and fast ion diffusion channels, stable morphology and systematic surface engineering. A series of interlinked multiphase Fe-doped MnO_2 nanostructures were successfully engineered by a facile hydrothermal synthesis. The typical Fe-doped MnO_2 electrode shows the significantly improved specific capacitance (267.0 F g^{-1}), rate capability (68.6 % capacitance retention from 0.1 to 5 A g^{-1}) and cycle life (100 % maintained after 2000 cycles) compared to the pure MnO_2. Furthermore, all-solid-state symmetric supercapacitor based on the Fe-doped MnO_2 electrodes was fabricated and studied for evaluating the practical application.

Experimental

Synthetic procedures

All the reagents used in the experiment were of analytical grade and used without further purification. In a typical experiment, 8 mmol $MnSO_4 \cdot H_2O$, 8 mmol $(NH_4)_2SO_4$ and 15 mmol $(NH_4)_2S_2O_8$ were dissolved in 30 ml deionized water. Different molar ratio of $Fe_2(SO_4)_3$ were used as dopant reagents of Fe introduced in the above solution. After magnetic stirring for 30 min, the homogeneous mixture solution was transferred to a 50 ml stainless Teflon-lined autoclave and treated hydrothermally at 120 ℃ for 12 h. Finally, the resulting precipitate was washed several times by deionized water and dried at 60 ℃ for 10 h. To investigate the influence of doping concentration, the different molar ratios (1:16, 1:8, 1:4, 1:2, 1:1 and 2:1) of Fe^{3+} and Mn^{2+} in the initial solution were synthesized, and the products designated as MnO_2-1/16, MnO_2-1/8, MnO_2-1/4, MnO_2-1/2, MnO_2-1/1, and MnO_2-2/1. The pure MnO_2 was denoted as MnO_2-0.

Characterization

The X-ray diffraction (XRD) patterns were performed on a Rigaku D/MAX-2500 X-ray powder diffractometer with Cu Kα radiation (λ=0.154 nm). Transmission electron microscopy (TEM) and high resolution TEM (HRTEM) images were examined under a transmission electron microscope (FEI Tecnai F20) at an acceleration voltage of 200 kV. Field-emission scanning electron microscope (FESEM) images and energy dispersive spectroscopy (EDS, OXFORD 51-XMX) data of the samples were carried out on a ZEISS SUPRA 55 SEM. X-ray photoelectron spectroscopy (XPS) data were obtained with an AXIS Ultra DLD electron spectrometer. Raman spectra were acquired using a microscopic confocal Raman spectrometer (HORIBA HR800) with an Nd:YAG laser at a wavelength of 532 nm. The nitrogen adsorption-desorption isotherms were measured at 77 K on a Autosorb-iQ2-MP analyzer. The specific surface area was calculated from the adsorption curve according to the Barrett-Joyner-Halenda (BJH) method.

Electrochemical measurements

Typically, a homogenized slurry containing 80 wt% prepared Fe-doped MnO_2 powders, 10 wt% acetylene black and 10 wt% polytetrafluorene ethylene (PTFE) was coated onto the current collector of nickel foam (1.0 cm×1.0 cm), and then dried overnight at 80 ℃. The mass loading of the electrode material is about 5 mg. The electrochemical performances were tested in a three-electrode configuration with platinum foil counter electrode and saturated calomel reference electrode (SCE) in 1 M Na_2SO_4 aqueous electrolyte. Cyclic voltammetry (CV) and galvanostatic charge/discharge (GCD) measurements were conducted on a CHI 660D electrochemical workstation. The electrochemical impedance spectroscopy (EIS) was carried out with a superimposed 5 mV sinusoidal voltage in the frequency range of 0.01 Hz-100 kHz.

The specific capacitances (C_S) were calculated from the galvanostatic discharge curves according to the following equation:

$$C_s = \frac{I}{m \cdot \left(\frac{\Delta U}{\Delta t} \right)} \quad (1)$$

where C_s (F g^{-1}) is the gravimetric capacitance of the electrode material, I (A) is the constant current applied, $\Delta U/\Delta t$ (V s^{-1}) is the linear slope of the discharge curve after the initial IR drop and m (g) is the active material mass of working electrode.

The all-solid-state symmetric supercapacitor (SSC) device was assembled by two separating MnO_2-1/8 electrodes with a NKK separator. Polyvinyl alcohol (PVA)/KOH gel was used as the electrolyte which was prepared by adding 3.0 g KOH and 3.0 g PVA (Aladdin 1788) to 30 mL of distilled water and heating at 80 ℃ for 2 h under magnetic stirring. After the solution became clear and uniform, the electrodes were soaked in the PVA/KOH solution and then allowed to solidify at room temperature for 2 h. The electrodes were assembled together and kept 45 ℃ for 12 h to remove excess water in the electrolyte. The thickness of the all-solid-state SSC was measured to be 1 mm and the active material mass was about 10 mg cm^{-2}.

The volumetric capacitances (C_V, F cm^{-3}) were caluculated from the galvanostatic discharge curves of the all-solid-state SSC using the following equations:

$$C_V = \frac{I}{V \cdot \left(\frac{\Delta U}{\Delta t}\right)} \quad (2)$$

The volumetric energy density (E, W h cm^{-3}) and power density (P, W cm^{-3}) of the device were obtained as follows:

$$E = \frac{1}{2} C_V (\Delta U)^2 \quad (3)$$

$$P = \frac{1}{4} \cdot \frac{(\Delta U)^2}{VR} \quad (4)$$

$$R = \frac{\Delta U_{drop}}{2I} \quad (5)$$

where ΔU (V) is the cell voltage window, R is the internal resistance of the device estimated from the initial IR drop (ΔU_{drop}) of the discharge curve at a constant current density I (A cm^{-3}), and V (cm^3) is the volume of the total device.

Results and discussion

The morphologies of Fe-doped MnO_2 with different precursor molar ratios were investigated by SEM. The pure MnO_2 sample (MnO_2-0) shown in Fig. 1(a-b) possesses a glomerate linear structure and these one-dimensional nanowires have uniform diameter of ~20 nm. When a low amount of Fe^{3+} was introduced (MnO_2-1/16), the sample is still clustered nanowires but with the nucleation induced by Fe^{3+} (Fig. 1(c-d)). Fig. 1(e-f) display the microstructure of MnO_2-1/8. Clearly, its morphology transforms to the urchin-shaped microspheres with plenty of nanorods radiating from the spherical shells. The microspheres have uniform size of 2-3 μm. As the amount of Fe^{3+} continuously increased (MnO_2-1/4), the length and density of the nanorods severely degrade, which can be obviously seen from the Fig. 1(g-h). For the MnO_2-1/2, isolated 3D clew-like microspheres with a diameter of 1-2 μm was observed in Fig. 1(i-j). High magnification SEM reveals that these microspheres (including MnO_2-1/8, MnO_2-1/4 and MnO_2-1/2) have a hierarchical nanostructure assembled by numerous interconnected nanoflakes, resulting in a porous structure with an enormous amount of cavities between adjacent flakes. In fact, these microspherical products are of obviously hollow structures (Supporting Information, Fig. S1†) and have considerable surface area (Supporting Information, Table S2†), thus boding well for high specific capacitance. Further increasing the amount of Fe^{3+} (MnO_2-1/1), leads to the formation of irregular agglomerates with smaller diameters of 0.5-1 μm (Fig. 1(k-l)). When the doping ratio is increased to 2:1, the morphology hardly changes except for generating large ammoniojarosite ($(NH_4)Fe_3(SO_4)_2(OH)_6$) crystals (Supporting Information, Fig. S2†).

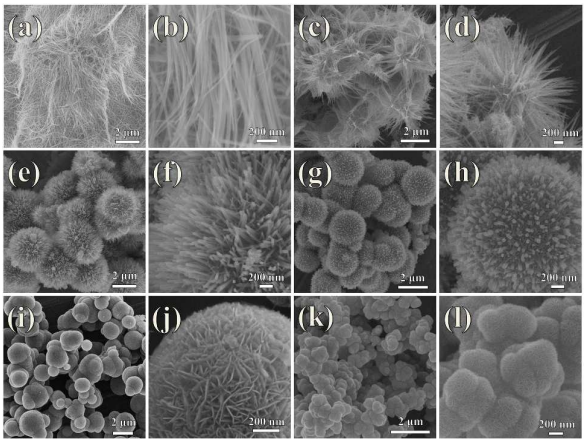

Fig. 1 SEM images of Fe-doped MnO_2 with different doping ratios. (a-b) MnO_2-0; (c-d) MnO_2-1/16; (e-f) MnO_2-1/8; (g-h) MnO_2-1/4; (i-j) MnO_2-1/2; (k-l) MnO_2-1/1.

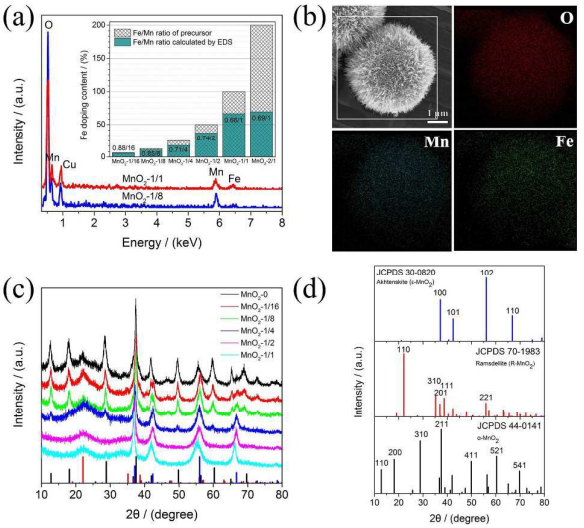

Fig. 2 (a) EDS spectra of MnO_2-1/8 and MnO_2-1/1, the inset gives the variation tendency of Fe^{3+} concentration; (b) elemental mapping of MnO_2-1/8; (c) XRD patterns of MnO_2-0 to MnO_2-1/1; (d) JCPDS cards of ε-MnO_2, R-MnO_2 and α-MnO_2.

Fig. 2(a) is the EDS spectra of typical Fe-doped MnO_2, which reveals that the samples are only composed of O, Mn and Fe (Cu is from the copper substrate). It is anticipated that the calculated Fe/Mn ratios are partly lower than the doping values. And the maximum Fe^{3+} concentration is no more than 0.66/1 (Fe/Mn) (Inset of Fig. 2(a)). The elemental line scanning and mapping of O, Mn and Fe for the representative samples (Fig. S3† and Fig. 2(b)) clearly illustrate that the Fe element is uniformly distributed throughout the microspheres. The phase evolution is monitored by the XRD measurement (Fig. 2(c)). The pattern of MnO_2-0 shows that it consists of a mixed phase. All diffraction peaks can be assigned to the tetragonal phase of α-MnO_2 (JCPDS 44-0141) and the orthorhombic phase of ramsdellite-MnO_2 (R-MnO_2) (JCPDS 70-1983). After incorporation of Fe^{3+} into MnO_2, the peak intensity of α-MnO_2 becomes weak and the phase of ε-MnO_2 appears. Increasing the Fe^{3+} feed to 1:2 (MnO_2-1/2), the XRD peaks are much blunter than that of MnO_2-0, which suggests that MnO_2-1/2

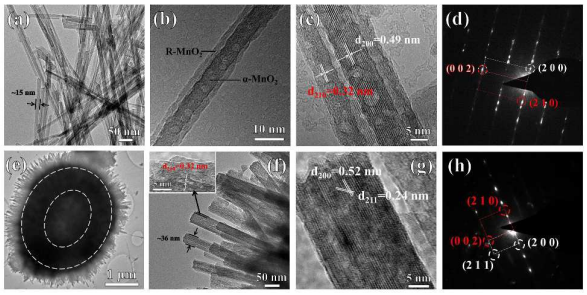

Fig. 3 (a-b) TEM images with different magnifications, (c) HRTEM image and (d) SAED pattern of MnO_2-0; (e-f) TEM images with different magnifications, (g) HRTEM image and (h) SAED pattern of MnO_2-1/8. (the white and red words stand for the α-MnO_2 phase and R-MnO_2 phase, respectively)

has a lower crystallization due to the disorders or defects of lattices resulting from the excessive Fe dopants. On the other hand, obviously, the phase of α-MnO_2 disappeared, replaced by the ε-MnO_2 phase (JCPDS 30-0820), which indicates that Fe^{3+} results in the phase transition from α-MnO_2 to ε-MnO_2. [28] Comparing the XRD patterns of different samples, it is observed that all samples contain the ramsdellite phase (as a result of excessive acid erosion [30]) and there is no iron-related phase in any of Fe-doped MnO_2, therefore suggesting that there are three MnO_2 phases (α, R and ε) in the low-concentration doped samples (MnO_2-1/16, MnO_2-1/8 and MnO_2-1/4). Fig. 2(d) gives their standard JCPDS cards. The structure and crystallization as well as chemical composition and metal oxidation state of the Fe-doped MnO_2 are also supported by Raman spectroscopy and XPS results, respectively (Supporting Information, Fig. S4†-S6†).

TEM provides a deeper insight into the microstructures and phases of typical samples. Fig. 3(a) depicts the ultrasonic dispersed MnO_2-0 nanowires, which exhibit the uniform diameter of ~15 nm as the SEM observations. Interestingly, these nanowires present the clearly hierarchical core-shell nanostructure (Fig. 3(b)). The peripheral R-MnO_2 is formed by the acid digestion of α-MnO_2 and with the possibility of epitaxial growth from the edge of alpha phase. [30, 31] HRTEM and SAED pattern from a single nanowire shown in Fig. 3(c-d) reveal its [001] growth direction. The well-resolved lattice fringes from the core and shell regions, manifestly correspond to the (200) planes of α-MnO_2 and the (210) planes of R-MnO_2, respectively. Moreover, two sets of diffraction patterns for the tetragonal α-MnO_2 and orthorhombic R-MnO_2 and thus confirms the single-crystalline nature of the core-shell nanowires. This result is also consistent with the structure determined by XRD. In the TEM image of MnO_2-1/8 (Fig. 3(e)), the border and center of the microsphere show distinguishable brightness contrast, further confirming its hollow nature. Microspherical surface is uniformly covered by radial nanorods of ~500 nm in length and ~36 nm in diameter. From the further magnified image (Fig. 3(f)), the R phase still can be observed on the edge section of the nanorods. Specially, numerous mesopores ranging from 2 to 5 nm in size are distributed throughout the nanorods (Fig. S8(b) gives the pore size distribution curves). This hollow spherical structure with unique porous branching is good for electrolyte penetration and ion/electron transfer, which may result in superior electrochemical properties. The HRTEM image (Fig. 3(g)) shows that the main lattice fringes match well to the (200) and (211) crystal faces of α-MnO_2. It is important to note that the interplanar distances of the (200) crystal planes enlarge from 0.49 nm to 0.52 nm but the (211) planes barely change. The doped structure is more consistent with another tetragonal α-MnO_2 (JCPDS 53-0633) than the MnO_2-0 (JCPDS 44-0141). The SAED patterns (Fig. 3(h)) again confirm the single crystalline nature of multiphase coexistent MnO_2-1/8 (the diffraction pattern of ε phase is too weak to be identified). The TEM of MnO_2-1/1 exhibits the irregular stacking structure made from many intersecting nanoflakes (Supporting Information, Fig. S7(a)†). From the HRTEM images, a poor crystallization can be observed as revealed by the "low-resolution" fringes in Fig. S7(b)†. The interplanar distances in different grains are measured to be 0.24 and 0.40 nm, which are in accord with the main lattice spacing of hexagonal ε-MnO_2 and orthorhombic R-MnO_2, respectively, verifies the compound phase of MnO_2-1/1. Correspondingly, a polycrystalline SAED pattern consistent with the two phases is depicted in the Fig. S7(c)†.

On the basis of experimental results, we now try to explain the phase transformation process and growth mechanism of the Fe-doped MnO_2. Initially, the doped Fe^{3+} would occupy the tunnels of α-MnO_2 preferentially as a interstitial atom [32]. These Fe^{3+} in the tunnel structures could bond to the defective [MnO_x]. Then the another Fe^{3+} access the slightly deformed tunnels and repeat the bonding process until the (2×2) tunnel vanishes. It may explain why the diameters of the tunnels grow larger at the MnO_2-1/8. Namely, a number of Fe^{3+} as the heterogeneous components go into the tunnel and gradually change the growing trend of MnO_2 (α-MnO_2) to ε-MnO_2 with the continuous collapse and recombination [33, 34]. At a later stage, most Fe^{3+} substitute as Mn^{4+} in the ε phase because of their similarities. It is the reason of so high Fe concentration was detected in the ε-MnO_2 specimen, the interplanar distances of ε-MnO_2 continually increased with the doping

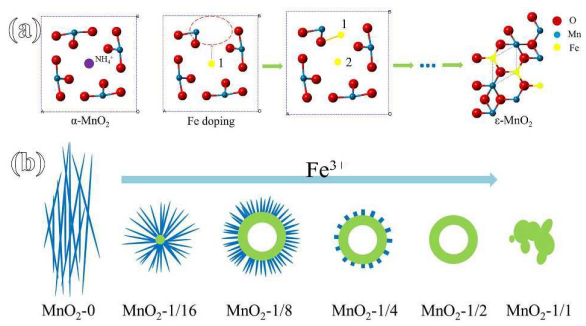

Fig. 4 (a) The structure schematic of the phase transition process from α-MnO_2 to ε-MnO_2; (b) Schematic of microstructure of Fe-doped MnO_2 with the Fe^{3+} increasing.

concentration (from XRD results and the atom radius of Fe^{3+} (~63 pm)＞Mn^{4+} (~53 pm)) and the crystallinity of ε phase is so low (amount of defects, like oxygen vacancy generated by Mn^{4+}→Fe^{3+}). This process is illustrated in the Fig. 4(a). Moreover, the decreased pH of solution also plays a role for the phase transition [35]. The presence of R-MnO_2 is independent with the Fe doping, but the Fe doping affects its crystallinity.

In order to correlate the structural and morphological characteristics of Fe-doped MnO_2 with their electrochemical properties, the cyclic voltammetry (CV) and galvanostatic charge/discharge (GCD) measurements were performed using a three-electrode configuration in 1 M Na_2SO_4 aqueous electrolyte. All CV curves exhibit a nearly rectangular shape at scan rate of 5 mV s^{-1} (Supporting Information, Fig. S9(a)†), implying the good capacitive behavior. Apparently, most CV curves of Fe-doped MnO_2 show much bigger curve area than that of pure MnO_2, suggesting that Fe doping has a dramatically positive effect on promoting the capacitance. Fig. S9(b)† displays the charge-discharge curves of the samples at current density of 0.1 A g^{-1}. The linear slopes and symmetrical triangle shape corroborate superior coulombic efficiency and excellent reversibility. The specific capacitances calculated according to Eq. (1) for Fe-doped MnO_2 with different Fe/Mn atomic ratios of 0, 1/16, 1/8, 1/4, 1/2, 1/1, 2/1 are 120.3, 155.9, 267.0, 264.8, 275.6, 283.4 and 170.6 F g^{-1}, respectively, at 0.1 A g^{-1} (Supporting information, Fig. S9(d)†). As expected, the suitable doping ratios (1/8-1/1) give a longer discharge time. It is noteworthy that excess Fe doping can decline the specific capacitance, possibly due to the little contribution of ammoniojarosite and much low crystallinity of MnO_2-2/1. The highest specific capacitance (283.4 F g^{-1}) is over doubled than that of pure MnO_2 (120.3 F g^{-1}), and much higher than other metal doped MnO_2 materials published recently (summarized in Supporting Information, Table S4†).

A more detailed set of CV and GCD curves of MnO_2-1/8 at various rates are shown in Fig. 5(a-b). The CV curve maintains a quasi-rectangular shape even at a scan rate of 100 mV s^{-1}, demonstrating rapid capacitive response in the high areal mass loading electrode. On the other side, the CV curve of a pseudocapacitive material keeps "rectangle-shape" at the low rate of 5 mV s^{-1}, which signifies that the electron transfers in the as-prepared MnO_2-1/8 are fairly rapid. [29] The charge/discharge curves of MnO_2-1/8 are almost symmetric and linear triangular profile in the current density range of 0.1 to 2.0 A g^{-1}. Meanwhile, the initial voltage drop is only 0.016 V at 1.0 A g^{-1}, much smaller than that of its counterparts (Fig. 5(c) and Fig. S10(b)†), which reveals its lower inner resistance and weaker polarization, by virtue of a balanced Fe dopant in MnO_2. Moreover, the MnO_2-1/8 retains the high specific capacitances of 267.0 and 183.1 F g^{-1} at charge/discharge current densities of 0.1 and 5.0 A g^{-1}, respectively, corresponding to a 68.6 % capacitance retention. This excellent rate capability, which is very crucial for high-power supercapacitor applications, is much larger than that of MnO_2-0 (38.2%), MnO_2-1/1 (54.6%) and others (Fig. 5(c) and Fig. S9(c)†). Additionally, the CV profile of MnO_2-1/1 recorded at 200 mV s^{-1} is obviously distorted compared with the MnO_2-1/8 (Fig. 5(d)). The result also implies superior ion response of MnO_2-1/8.

The enhanced electrochemical properties of Fe-doped MnO_2 were further confirmed by EIS test (Fig. 5(e) and Fig. S10(a)†). Comparatively, MnO_2-1/8 and MnO_2-1/1 both have quite lower equivalent series resistance (the high frequency

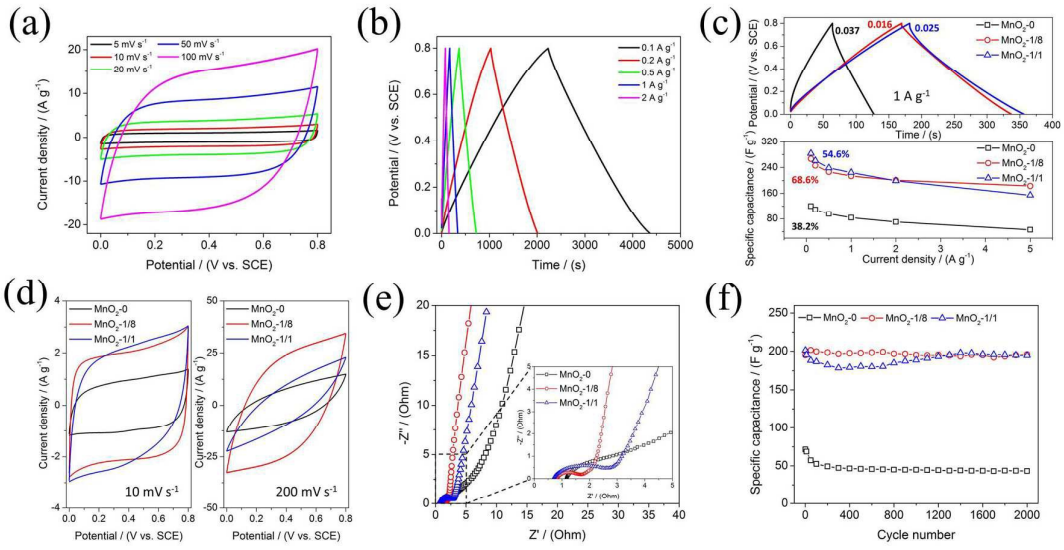

Fig. 5 (a) CV curves of MnO_2-1/8 at different scan rates; (b) GCD curves of MnO_2-1/8 at different current densities; (c) GCD curves at 1 A g^{-1} and capacitance values at different current densities of MnO_2-0, MnO_2-1/8 and MnO_2-1/1, respectively; (d) CV curves of MnO_2-0, MnO_2-1/8 and MnO_2-1/1 at 10 mV s^{-1} and 200 mV s^{-1}, respectively; (e) EIS analysis of MnO_2-0, MnO_2-1/8 and MnO_2-1/1; (f) cycling performance of MnO_2-0, MnO_2-1/8 and MnO_2-1/1 (2000 cycles at a current density of 2 A g^{-1}).

intersection of the Nyquist plot in the real axis), representing that Fe doping has a evident effect on electric conductivity. What's more, MnO_2-1/8 presents a much reduced charge transfer resistance (the diameter of the semicircle at the high-medium frequency) than that of MnO_2-1/1 (as well as magnitude smaller than MnO_2-0). It is revealed that MnO_2-1/8 electrode has faster reaction kinetics than other counterparts, due to the more conductive and active system constructed by the multiphase crystal structure. The almost vertical line of Fe-doped MnO_2 (distinctly steeper than pure MnO_2) is indicative of an ideal capacitive behavior and very low electrolyte diffusion resistance. This can be attributed to the existence of continuous ion transport channels in our doped samples. Table S3† in Supporting Information gives the impedance parameters calculated from the equivalent circuit of Fig. S11†. High areal mass loading and excellent cycling stability also constitute a key performance indicator for a pseudocapacitor electrode in practice. Cyclic test were carried out for over 2000 cycles at 2 A g^{-1}. The results plotted in Fig. 5(f) present that the MnO_2-1/8 and MnO_2-1/1 electrode exhibit almost no degradation and only 3.2% capacitance loss in performance after 2000 cycles, respectively, which are much better than the 39.4% capacitance loss for pure MnO_2 electrode. The amazing results can be ascribed to the outstanding structure stability of the Fe-doped MnO_2.

The all-solid-state symmetric supercapacitor (SSC) was assembled for evaluating the potential of the multiphase Fe-doped MnO_2 electrode material (Supporting Information, Fig. S13†). As anticipated, the device presents a competitive volumetric capacitance of 14.65 F cm^{-3} at the current density of 1 mA cm^{-2}. The cycling performance of the SSC device, which was investigated using a cyclic charge-discharge test at a current density of 10 mA cm^{-2}, is depicted in the Fig. S13(e). The acceptable capacitance retention (about 74%) and favorable coulombic efficiency after 1000 cycles confirm the capacity of the MnO_2-1/8 as a real device. Furthermore, based on the Ragone plot (Fig. S13(f)), the all-solid-state unit delivered the maximum energy density of 1.30 mW h cm^{-3} with a power density of 0.125 W cm^{-3}, which is obviously higher than the reported values of some flexible SSCs, even asymmetric supercapacitor (ASC) devices [36-38].

We propose a detailed explanation for the excellent supercapacitive properties of Fe-doped MnO_2 (MnO_2-1/8) as follows. It is known that the doped metal atoms as electron donors can effectively improve the electronic structure, which intrinsically elevates the electrical conductivity and capacitance values of MnO_2 material. [23] This part of work has been systematically studied by the earlier reports. [24] On this basis, the crystal structure, crystallinity and morphology also play a pivotal role in the electrochemical performance of Fe-doped MnO_2 electrodes.

As mentioned above, three MnO_2 crystallographic phases (α-MnO_2, R-MnO_2 and ε-MnO_2) were found in one particle simultaneously in our samples. In the structural perspective of Fig. 4(a), α-MnO_2 is a typical (2×2) tunnel structure material, which is suitable for insertion/extraction of alkali cations. For this reason, its outstanding electrochemical properties have been demonstrated in numerous studies. [39] However, α-MnO_2 framework structure form is usually stabilized by the large cations, such as Ba^+, K^+ and NH_4^+ ions, which locates within the large (2×2) channel. [30] Because these cations somewhat impede the diffusion of electrolyte ions during the electrochemical operation, efforts were made to develop more iron channels, [32] namely, a crystallographically interconnected composite structure of two coordinated MnO_2 phases. [30, 31] R-MnO_2 with smaller (2×1) channels, provides greater stability than α-MnO_2. But an anisotropic expansion and contraction of the unit cell parameters during cations insertion/extraction causes the structural damage and loss of capacity on cycling. [40] Given their respective structural limitations, it is anticipated that the existence of interlinked α-MnO_2 and R-MnO_2 may accommodate large amount of ions to intercalate without structure destruction. Next we definitely needed a tool known as "defects (oxygen vacancy)" for interconnecting these channels. ε-MnO_2 (1×1), which was found to be most promising for oxygen reduction reaction (ORR) catalysis, shows more structural faults (de Wolff faults) and structural defects (micro-twinning) among the available polymorphs. [41, 42] On the one hand these active sites should also be very benefit for the pseudocapacitive reaction, on the other hand pervasive ε-MnO_2 provides a large number of defects what we need. In our studies, Fe doping of MnO_2 provides an effective way to induce a phase transformation from α phase to ε phase. With the addition of the acid erosion, a selected multiphase MnO_2 which combines the advantages of each phases can be achieved responsibly.

In our case, the optimized Fe/Mn atomic ratio is considered to be the 1/8. It is worth noting that the overdoping of hetero atoms could result in superfluous defects and too low crystallinity, so the capacity of MnO_2-1/1 did not show the superiority as it's the highest specific surface area (300.484 m^2 g^{-1}). Additionally, excess Fe^{3+} in MnO_2 would obstruct the insertion/extraction of alkali cations. This is why the rate capability of MnO_2-1/4 to MnO_2-2/1 gradually decreases with doping content. At the same time, MnO_2 experiences a series of morphology changes. Fig. 4(b) summarizes the microstructure evolvement of Fe-doped MnO_2. For MnO_2-0, even regardless of its terrible conductivity, these aggregated nanowires result in decreased surface area (106.668 m^2 g^{-1}) and electrochemical activities. With Fe^{3+} concentration increasing, this hierarchical microsphere structure (MnO_2-1/8 to MnO_2-1/1) constituted by nanoflakes, allowing enlarged specific surface area (Supporting Information, Table S2†), increased pore size and volume, shortened diffusion distance and highly stable morphology, is convenient for superb specific capacitance and cycle performance. What is more, this special ion-buffering reservoir of hollow microsphere is very beneficial to the electrochemical stability. Considering MnO_2-1/8, by growing directly from the microsphere "core", the entirely exposed nanorods "shell" with plenty of mesopores (Supporting Information, Fig. S8†) can facilitate the fast cations intercalation into MnO_2 layered structure and minimize transport resistance, thus enhanced electrochemical kinetics and high-rate performance.

Given the above, it is believed that a synergistic contribution accounts for the superior electrochemical performances of MnO_2-1/8. Namely, moderated Fe doping improves electric conductivity, interlinked multiphase structure promotes the ions/electrons transport kinetics and stability, 3D hollow spherical architecture provides firm structure and ion buffering reservoirs, and hierarchical porous texture helps for fast ion accommodation. Although, the specific capacitance is still lower than that of some noble metal (like, Au) doped MnO_2.[43] Impressively, the areal mass loading of our Fe-doped MnO_2 reached as high as 5 mg cm^{-1} with such encouraging performances. It will be more advantageous in practical application.

Conclusions

In summary, we propose an avenue for realizing a fast, active and stable electrolyte ions insertion/extraction process to enhance the electrochemical performances of materials. A series of interlinked multiphase (including α-MnO_2 , R-MnO_2 and ε-MnO_2) Fe-doped MnO_2 nanostructures were successfully synthesized by a simple hydrothermal method. Balanced Fe doping is proven to be a promising measure for an advantageous hierarchical multiphase MnO_2. The synergy of lower Faraday resistance, multiphase porous composition and integrated hollow microspherical architecture results in the outstanding electrochemical performances of Fe-doped MnO_2. The typical sample (MnO_2-1/8) with mass-loading of ~5 mg cm^{-2} exhibited a superior specific capacitance (267.0 F g^{-1} at 0.1 A g^{-1}), outstanding rate capability (68.6% capacitance retention with current density increasing from 0.1 to 1 A g^{-1}), and excellent cycling stability (100% retention after 2000 cycles at 2 A g^{-1}). Meantime, the typical sample-based all-solid-state symmetric supercapacitor exhibits a high energy density of 1.30 mW h cm^{-3} and a maximum power density of 0.291 W cm^{-3}. Hence, it is expected that this convenient and scalable method provides an attractive way to develop the cost-effective, environmentally benign and high-performance electrode materials for supercapacitor.

Acknowledgements

We appreciate the financial supports of the National Natural Science Foundation of China (Grant No. 61373072), the Fundamental Research Funds for the Central Universities: FRF-AS-13-004A and FRF-BR-14-024A and Beijing Higher Education Young Elite Teacher Project YETP0390.

References

1 F. Bonaccorso, L. Colombo, G. Yu, M. Stoller, V. Tozzini, A. C. Ferrari, R. S. Ruoff and V. Pellegrini, *Science*, 2015, **347**, 1246501.
2 X. Yang, C. Cheng, Y. Wang, L. Qiu and D. Li, *Science*, 2013, **341**, 534-537.
3 X. Xia, D. Chao, C. F. Ng, J. Lin, Z. Fan, H. Zhang, Z. X. Shen and H. J. Fan, *Mater. Horiz.*, 2015, **2**, 237-244.
4 G. Wang, L. Zhang and J. Zhang, *Chem. Soc. Rev.*, 2012, **41**, 797-828.
5 P. Simon and Y. Gogotsi, *Nat. Mater.*, 2008, **7**, 845-854.
6 C. Liu, F. Li, L. P. Ma and H. M. Cheng, *Adv. Mater.*, 2010, **22**, E28-E62.
7 R. S. Devan, R. A. Patil, J. H. Lin and Y. R. Ma, *Adv. Funct. Mater.*, 2012, **22**, 3326-3370.
8 H. Wang, H. S. Casalongue, Y. Liang and H. Dai, *J. Am. Chem. Soc.*, 2010, **132**, 7472-7477.
9 S. J. Bao, C. M. Li, C. X. Guo and Y. Qiao, *J. Power Sources*, 2008, **180**, 676-681.
10 N. Yu, M. Q. Zhu and D. Chen, *J. Mater. Chem. A*, 2015, **3**, 7910-7918.
11 J. Chmiola, C. Largeot, P. L. Taberna, P. Simon and Y. Gogotsi, *Science*, 2010, **328**, 480-483.
12 C. Zhu, P. Yang, D. Chao, X. Wang, X. Zhang, S. Chen, B. K. Tay, H. Huang, H. Zhang and W. Mai, *Adv. Mater.*, 2015, **27**, 4566-4571.
13 D. Chen, Q. Wang, R. Wang and G. Shen, *J. Mater. Chem. A*, 2015, **3**, 10158-10173.
14 E. Frackowiak, V. Khomenko, K. Jurewicz, K. Lota and F. Beguin, *J. Power Sources*, 2006, **153**, 413-418.
15 M. Toupin, T. Brousse and D. Bélanger, *Chemistry of Materials*, 2004, **16**, 3184-3190.
16 W. Wei, X. Cui, W. Chen and D. G. Ivey, *Chem. Soc. Rev.*, 2011, **40**, 1697-1721.
17 C. C. Hu and T. W. Tsou, *Electrochem. Commun.*, 2002, **4**, 105-109.
18 P. Ragupathy, D. H. Park, G. Campet, H. Vasan, S. J. Hwang, J. H. Choy and N. Munichandraiah, *J. Phys. Chem. C*, 2009, **113**, 6303-6309.
19 G. Yu, L. Hu, N. Liu, H. Wang, M. Vosgueritchian, Y. Yang, Y. Cui and Z. Bao, *Nano Lett.*, 2011, **11**, 4438-4442.
20 S. Chen, J. Zhu, X. Wu, Q. Han and X. Wang, *ACS Nano*, 2010, **4**, 2822-2830.
21 H. Kim, *J. Electrochem. Soc.*, 2002, **150**, D56-D62.
22 E. Machefaux, T. Brousse, D. B, eacute, langer and D. Guyomard, *J. Power Sources*, 2007, **165**, 651-655.
23 J. Kang, A. Hirata, L. Kang, X. Zhang, Y. Hou, L. Chen, C. Li, T. Fujita, K. Akagi and M. Chen, *Angew. Chem. Int. Edit.*, 2013, **52**, 1664-1667.
24 Z. Hu, X. Xiao, C. Chen, T. Li, L. Huang, C. Zhang, J. Su, L. Miao, J. Jiang and Y. Zhang, *Nano Energy*, 2015, **11**, 226-234.
25 X. Xia, D. Chao, Z. Fan, C. Guan, X. Cao, H. Zhang and H. J. Fan, *Nano Lett.*, 2014, **14**, 1651-1658.
26 T. Brousse, M. Toupin, R. Dugas, L. Athouël, O. Crosnier and D. Bélanger, *J. Electrochem. Soc.*, 2006, **153**, A2171-A2180.
27 B. Babakhani and D. G. Ivey, *J. Power Sources*, 2010, **195**, 2110-2117.
28 P. Yu, X. Zhang, D. Wang, L. Wang and Y. Ma, *Cryst. Growth Des.*, 2009, **9**, 528-533.
29 L. F. Chen, Z. Y. Yu, J. J. Wang, Q. X. Li, Z. Q. Tan, Y. W. Zhu and S. H. Yu, *Nano Energy*, 2015, **11**, 119-128.
30 C. S. Johnson, M. F. Mansuetto, M. M. Thackeray, Y. Shao-Horn and S. A. Hackney, *J. Electrochem. Soc.*, 1997, **144**, 2279-2283.
31 L. Trahey, N. K. Karan, M. K. Y. Chan, J. Lu, Y. Ren, J. Greeley, M. Balasubramanian, A. K. Burrell, L. A. Curtiss and M. M. Thackeray, *Adv. Energy Mater.*, 2013, **3**, 75-84.
32 L. Wu, F. Xu, Y. Zhu, A. B. Brady, J. Huang, J. L. Durham, E. Dooryhee, A. C. Marschilok, E. S. Takeuchi and K. J. Takeuchi, *ACS Nano*, 2015, **9**, 8430-8439.
33 Y. Yuan, S. M. Wood, K. He, W. Yao, D. Tompsett, J. Lu, A. Nie, M. S. Islam and R. Shahbazian-Yassar, *ACS Nano*, 2016, **10**, 539-548.
34 Y. Yuan, A. Nie, G. M. Odegard, R. Xu, D. Zhou, S. Santhanagopalan, K. He, H. Asayesh-Ardakani, D. D. Meng and R. F. Klie, *Nano Lett.*, 2015, **15**, 2998-3007.

35 X. F. Shen, Y. S. Ding, J. Liu, J. Cai, K. Laubernds, R. P. Zerger, A. Vasiliev, M. Aindow and S. L. Suib, *Adv. Mater.*, 2005, **17**, 805-809.
36 P. Yang, Y. Ding, Z. Lin, Z. Chen, Y. Li, P. Qiang, M. Ebrahimi, W. Mai, C. P. Wong and Z. L. Wang, *Nano Lett.*, 2014, **14**, 731-736.
37 X. Lu, M. Yu, G. Wang, T. Zhai, S. Xie, Y. Ling, Y. Tong and Y. Li, *Adv. Mater.*, 2013, **25**, 267-272.
38 W. Zilong, Z. Zhu, J. Qiu and S. Yang, *J. Mater. Chem. C*, 2014, **2**, 1331-1336.
39 S. L. Suib, *Accounts Chem. Res.*, 2008, **41**, 479-487.
40 M. M. Thackeray, M. H. Rossouw, R. J. Gummow, D. C. Liles, K. Pearce, A. De Kock, W. I. F. David and S. Hull, *Electrochim. Acta*, 1993, **38**, 1259-1267.
41 H. Wang, F. Yin, B. Chen and G. Li, *J. Mater. Chem. A*, 2015, **3**, 16168-16176.
42 Y. S. Ding, X. F. Shen, S. Gomez, H. Luo, M. Aindow and S. L. Suib, *Adv. Funct. Mater.*, 2006, **16**, 549-555.
43 J. Kang, A. Hirata, L. Kang, X. Zhang, Y. Hou, L. Chen, C. Li, T. Fujita, K. Akagi and M. Chen, *Angew. Chem.*, 2013, **125**, 1708-1711.